PROGRESS IN PHOTOVOLTAICS **WILEY**

Surface saturation current densities of perovskite thin films from Suns-photoluminescence quantum yield measurements

Robert Lee Chin[1] [iD] | Arman Mahboubi Soufiani[1] | Paul Fassl[2] |
Jianghui Zheng[1,3] | Eunyoung Choi[1] | Anita Ho-Baillie[1,3] [iD] | Ulrich W. Paetzold[2] |
Thorsten Trupke[1] [iD] | Ziv Hameiri[1] [iD]

[1]The University of New South Wales, Sydney, Australia

[2]Karlsruhe Institute of Technology (KIT), Karlsruhe, Germany

[3]The University of Sydney, Sydney, Australia

Correspondence
Robert Lee Chin, The University of New South Wales, Sydney, Australia.
Email: r.leechin@unsw.edu.au

Abstract

We present a simple yet powerful analysis of Suns-photoluminescence quantum yield measurements that can be used to determine the surface saturation current densities of thin film semiconductors. We apply the method to state-of-the-art polycrystalline perovskite thin films of varying absorber thickness. We show that the non-radiative bimolecular recombination in these samples originates from the surfaces. To the best of our knowledge, this is the first study to demonstrate and quantify non-linear (bimolecular) surface recombination in perovskite thin films.

KEYWORDS
implied voltage, non-radiative bimolecular, perovskite thin film, photoluminescence, photoluminescence quantum yield, radiative recombination, surface saturation current density

1 | INTRODUCTION

The photoluminescence quantum yield (PLQY) is an important opto-electronics measurement that can determine the implied photovoltaic quality of semiconductors.[1,2] PLQY measures the number of emitted photoluminescence (PL) photons, relative to the number of absorbed photons.[3] Often, PLQY is measured using a spectrometer,[1] such that the absolute *spectral* photon flux is obtained. When PLQY measurements are performed as a function of the light intensity or Suns (often named 'Suns-PLQY'), the excess carrier density, Δn, is varied providing information about the injection-dependence of the PLQY.[1]

For lead-based perovskite thin films (PTFs), PLQY measurements have been used to quantify the implied open-circuit voltage, iV_{OC}, and the iV_{OC} deficit, $\Delta iV_{OC,rad}$.[1,4–6] The iV_{OC} represents the quasi-Fermi level splitting (QFLS), or the maximum possible open-circuit voltage that could be obtained if the film were converted into a solar cell,[7] while $\Delta iV_{OC,rad}$ represents the loss in iV_{OC} relative to the radiative-limit due to defect-mediated or non-radiative recombination.[8] Suns-PLQY measurements have been used to quantify the non-radiative

recombination of PTFs via extraction of the implied efficiency potential and ideality factor, n_{id}.[1,9,10]

One of the main limitations of state-of-the-art PTFs is non-radiative bimolecular recombination (NRBR).[11] NRBR refers to recombination, which has the same injection-dependence or n_{id} as radiative bimolecular recombination ($n_{id} = 1$) but is mediated by defects, and hence does not produce photons, as expected in radiative recombination.[12] For context, the radiative recombination mechanism is described as 'bimolecular' because each recombination event involves the recombination of a free electron with a free hole.[13] NRBR in PTFs has been studied for more than half a decade, mostly using PLQY and/or time-resolved PL decay (TR-PL) measurements.[11,12,14–18] However, the exact nature and spatial origin of NRBR remains elusive. Previous suggestions included trap-Auger recombination inside the bulk,[12,19] yet first principles calculations from Staub et al. demonstrated that the trap-Auger mechanism is unlikely as the required bulk defect densities, N_t, is much larger than the experimentally determined value (above 10^{17} cm^{-3} compared to below 10^{16} cm^{-3}).[16] Brenes et al. subjected PTFs to light and atmospheric treatments and

observed an increase in PLQY and a concurrent decrease in the NRBR as determined from TR-PL.[18] They proposed that the treatments passivate surface states thereby reducing NRBR; however, no supportive evidence has been provided. Bowman et al. used combined TR-PL and Suns-PLQY measurement to calculate the *ratio* of the radiative to the total (radiative plus non-radiative) bimolecular recombination rates.[15] They hypothesised that shallow Shockley-Read-Hall (SRH) defect states may cause NRBR.

In this study, we use Suns-PLQY measurements to quantify and determine the spatial origin of NRBR in state-of-the-art PTFs. Our analysis involves converting Suns-PLQY data to dark implied current-density voltage (*iJ-V*) curves and subsequent extraction of the recombination current parameter, J_0, which is then used to quantify NRBR. To validate the results, PTFs of the same composition but varying absorber thickness, W, were used.

2 | EXPERIMENTAL METHODS

To prepare the perovskite $Cs_{0.05}FA_{0.79}MA_{0.16}Pb(I_{0.83}Br_{0.17})_3$ precursor solution, caesium iodide (CsI, Sigma-Aldrich), formamidinium iodide (FAI, GreatCell Solar Materials), lead iodide (PbI$_2$, TCI), methylammonium bromide (MABr, GreatCell Solar Materials), and lead bromide (PbBr$_2$, Sigma-Aldrich) were stoichiometrically weighed and dissolved in a mixed solvent of *N,N*-dimethylformamide (DMF, TCl) and dimethyl sulfoxide (DMSO, Alfa Aesar) (4:1 v/v) with different concentrations: 1.1 M (thick perovskite layer), 0.74 M (intermediate layer), and 0.5 M (thin layer). Glass substrates were sequentially cleaned with detergent, deionised water, acetone, and isopropanol. After that, the cleaned glass substrates were treated with ultraviolet ozone (UVO) for 15 min and then transferred into a nitrogen-filled glovebox. The precursor solution was spin-coated on the substrates at 2000 rpm for 20 s, followed by 6000 rpm for 30 s. During the spin-coating, 100 µL chlorobenzene (Sigma-Aldrich) was quickly dispensed 5 s prior to the end of the spin-coating process. The films were then annealed at 100°C for 10 min on a hot plate, producing a dense perovskite film as indicated by secondary electron microscopy (SEM) images. These images were also employed to assess the extent of substrate coverage, revealing a comprehensive coverage as clearly depicted in Section S1 of the Supporting Information. For brevity, this PTF composition is denoted 'Br17'.

Suns-PLQY measurements were carried out inside an integrating sphere (15 cm diameter, LabSphere), flushed with nitrogen gas. A green laser (LD-515-10MG, Roithner Lasertechnik) with a full-width-half-maximum (FWHM) spot size of ~778 µm was directed into the sphere via a small entrance port. An optical fibre collected the emission from the exit port of the sphere and guided it to the spectrometers (AvaSpec-2048×64TEC, Avantes). The spectral response was calibrated using a calibration lamp (HL-3plus-INT-Cal, Ocean Insight), giving a relative uncertainty of about ±3% in the spectral range of the PL emission (1.24 eV to 2.06 eV or 600 nm to 1000 nm). Raw measured spectra were converted to power spectra by normalising for integration time (0.2 s for most of the measurements). The PLQY was

TABLE 1 Thicknesses of the PTF samples used in this study, as determined by SE/T.

	Thick	**Intermediate**	**Thin**
W (nm)	469.3 ± 4.0	262.2 ± 2.0	159.5 ± 5.5

determined using the method described by de Mello et al.[3] The samples were placed at an angle of 15° with respect to the laser beam to avoid specular reflectance towards the entrance port. To stabilise both the spectral PL magnitude and shape, the samples were light-soaked at an intensity of ~30 Suns for 3 min, after which the Suns-PLQY measurements were performed.

Spectroscopy ellipsometry (SE) was used to determine the spectral absorptivity and thickness of the PTFs. An ellipsometer (M2000, J. A. Woollam) was used to measure the complex refractive index of the PTF on glass in the wavelength range of 210 to 1000 nm. The ratio of the change in the polarisation of the light reflected from the sample was measured in ambient air at incident angles of 55°, 65°, and 75° to establish a model for the room temperature optical constants of the Br17 PTF. For this purpose, the computer software WVASEVR[20] was used. To add an extra constraint on the ellipsometry fits, the experimental transmission spectrum of the measured samples, taken using a spectrophotometer (Lambda 1050, Perkin Elmer), was simultaneously fitted alongside the SE data. The curve fits are presented in Section S2 of the Supporting Information. The transfer matrix method (TMM) is used to calculate the PTF spectral absorptivity.[21] The thicknesses determined from SE and transmission (SE/T) are summarised in Table 1.

3 | ANALYSIS METHODS

The PLQY value, Φ_{PLQY}, is defined as the ratio of emitted PL photons to the absorbed excitation photons:

$$\Phi_{PLQY}(J_{rec}) = \frac{\int \phi_{PL}(\hbar\omega, J_{rec}) \, d\hbar\omega}{\phi_{ex}} \quad (1)$$

where $\phi_{PL}(\hbar\omega, J_{rec})$ is the *emitted* absolute spectral PL photon flux ($cm^{-2} \cdot s^{-1} \cdot eV^{-1}$) and ϕ_{ex} is the *absorbed* excitation photon flux ($cm^{-2} \cdot s^{-1}$). ϕ_{PL} is a function of the photon energy, $\hbar\omega$, and is specified at a particular value of ϕ_{ex}. The J_{rec} represents the current density due to the net recombination (generation), denoted 'rec', rate of excess charge carriers and is given by $J_{rec} = q \cdot \phi_{ex}$. It is noted that PTFs exhibit a significant fraction (~50%) of emission from the glass edges due to radiative recombination photons scattering from the non-planar PTF surface and waveguiding into the glass.[22] Therefore, this analysis requires that the Suns-PLQY measurements be performed inside a 4π integrating sphere.[3]

The Lasher-Stern Würfel (LSW) equation[7,23] relates $\phi_{PL}(\hbar\omega)$ to the iV_{OC}:

$$\phi_{PL}(\hbar\omega, J_{rec}, T) = \text{Abs}(\hbar\omega) \cdot \phi_{BB}(\hbar\omega, T) \cdot \exp\left[\frac{iV_{OC}(J_{rec})}{k_B T}\right] \quad (2)$$

where $\text{Abs}(\hbar\omega)$ is the spectral band-to-band absorptivity, $\phi_{BB}(\hbar\omega, T)$ is the blackbody spectral photon flux emitted into the full sphere (4π sr) at carrier temperature T, and $k_B T$ is the thermal energy. Equation (2) may be linearised to extract iV_{OC}[24–26]:

$$\ln\left[\frac{2\pi^2 \hbar^3 c_0^2}{(\hbar\omega)^2} \cdot \frac{\phi_{PL}(\hbar\omega, J_{rec})}{\text{Abs}(\hbar\omega)}\right] = \frac{1}{k_B T}[\hbar\omega - iV_{OC}(J_{rec})] \quad (3)$$

Ideally, plotting the left-hand-side of Equation (3) as a function of $\hbar\omega$ forms a straight line with a slope of $1/k_B T$ and a y-intercept of $-iV_{OC}/k_B T$.

Subsequently, the radiative-limited implied voltage, $iV_{OC,rad}$, can be determined from iV_{OC} and Φ_{PLQY}[8]:

$$iV_{OC,rad}(J_{rec}) = iV_{OC}(J_{rec}) - k_B T \cdot \ln[\Phi_{PLQY}(J_{rec})] \quad (4)$$

$iV_{OC,rad}$ represents iV_{OC} when no non-radiative recombination is present and the term $\Delta iV_{OC,rad} = k_B T \cdot \ln(\Phi_{PLQY})$ is the implied open-circuit deficit relative to the radiative-limit. Note that Φ_{PLQY} is always <1, and thus, $\Delta iV_{OC,rad}$ is always positive. J_{rec} plotted as a function of iV_{OC} represents the dark iJ-V curve of the PTF: $J_{rec}(iV_{OC}) = iJ(iV)$, where $iJ(iV)$ is the implied dark current-density as a function of the implied voltage. The iJ-iV curve can be decomposed into the iJ-iV curves due to radiative (iJ_{rad}) and non-radiative (iJ_{nr}) recombination, respectively:

$$iJ(iV) = iJ_{rad}(iV) + iJ_{nr}(iV) \quad (5)$$

J_{rec} plotted as a function of $iV_{OC,rad}$ represents the radiative dark iJ-iV curve: $J_{rec}(iV_{OC,rad}) = iJ_{rad}(iV)$. As the radiative recombination has a n_{id} of unity, the radiative dark iJ-iV curve can be modelled as

$$iJ_{rad}(iV) = J_{0,rad} \cdot \left(\exp\left[\frac{iV}{k_B T}\right] - 1\right) \quad (6)$$

where $J_{0,rad}$ is the radiative recombination parameter ($A \cdot cm^{-2}$).[27] If NRBR is the dominant non-radiative recombination mechanism, $iJ_{nr}(iV)$ is

$$iJ_{nr}(iV) = J_{0,nr} \cdot \left(\exp\left[\frac{iV}{k_B T}\right] - 1\right) \quad (7)$$

where $J_{0,nr}$ is the recombination parameter associated with NRBR ($A \cdot cm^{-2}$). Combining Equations (5), (6), and (7), $iJ(iV)$ can be expressed as

$$iJ(iV) = (J_{0,rad} + J_{0,nr}) \cdot \left(\exp\left[\frac{iV}{k_B T}\right] - 1\right) \quad (8)$$

By varying W, one can determine the spatial origin of $J_{0,nr}$. Accounting for NRBR at the surfaces and inside the bulk,[27] $J_{0,nr}$ can be expressed as

$$J_{0,nr} = J_{0,s} + q \cdot W \cdot n_i^2 \cdot B_{bulk,nr} \quad (9)$$

where $J_{0,s}$ and $J_{0,bulk,nr} = q \cdot W \cdot n_i^2 \cdot B_{bulk,nr}$ are the non-radiative saturation current densities for the surface and the bulk NRBR, respectively. $B_{bulk,nr}$ is the bulk NRBR coefficient,[11,12,15,18] and n_i is the intrinsic carrier density.[28]
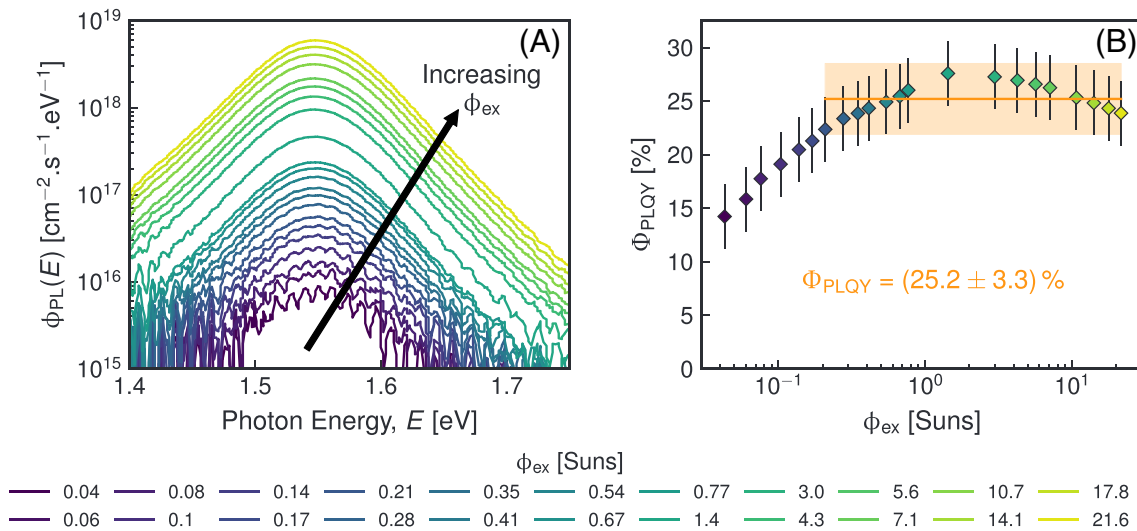
FIGURE 1 (A) $\phi_{PL}(\hbar\omega)$, colour coded to ϕ_{ex}. The shaded regions represent the measurement uncertainty due to the absolute calibration (±3%) and spectrometer dark noise. (B) Φ_{PLQY} versus ϕ_{ex}. The orange region shows the approximate plateau value of the $\Phi_{PLQY} = (25.2 \pm 3.3)\%$, indicating the presence of NRBR.

4 | RESULTS AND DISCUSSION

Unless otherwise stated, all the presented measurement results are for the intermediate PTF. Figure 1A illustrates the Suns-PLQY measurements, represented as $\phi_{PL}(\hbar\omega)$, which cover nearly three orders of magnitude of ϕ_{ex}. Throughout the wide range of Suns, we observed no changes in the shape of $\phi_{PL}(\hbar\omega)$, indicating the reasonably stable composition of the studied PTFs. Additionally, the absence of low-energy shoulders in $\phi_{PL}(\hbar\omega)$ suggests that phase segregation[29] does not have a significant macroscopic impact on the Suns-PLQY measurements of the investigated samples.
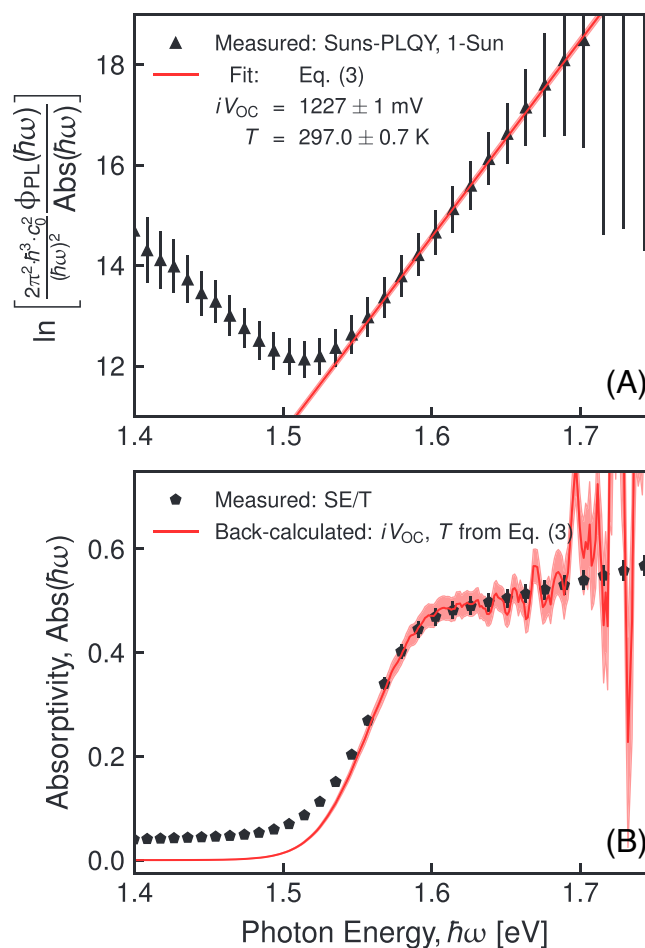
Figure 1B shows PLQY as a function of ϕ_{ex} in Suns, where 1-Sun is defined as equivalent to a photogenerated current density, J_L, of 18.7 mA·cm^{-2} (see Section S3 of the Supporting Information). We observe Φ_{PLQY} remains consistently within $(25.2 \pm 3.3)\%$ over almost two orders of magnitude ($\phi_{ex} > 0.2$ Suns). Φ_{PLQY} may be defined additionally to Equation (1) as the external radiative recombination rate ($R_{rad,ext}$) relative to the net recombination rate (R_{tot}): $\Phi_{PLQY} = R_{rad,ext}/R_{tot}$.[30] A plateau of the PLQY indicates that the dominant recombination mechanism has the same injection dependence as the radiative recombination. The difference between this plateau value and unity is attributed to non-radiative recombination. Thus, NRBR can be identified in Suns-PLQY as a plateau of Φ_{PLQY} ($\Phi_{PLQY} < 1$) with changing Suns. This constancy suggests that the dominant non-radiative recombination mechanism is indeed NRBR.

Figure 2A demonstrates the application of Equation (3) to the 1-Sun $\phi_{PL}(\hbar\omega)$ of the intermediate PTF. The fitting region was carefully selected to ensure a high signal-to-noise ratio (SNR) and avoid the 'edge artefact' caused by low-energy photons scattered at the film surfaces and guided towards the glass edges.[22] The fit quality appears to be good, reflected by the fitted iV_{OC} and temperature uncertainties of only ± 1 mV and ± 0.7 K, respectively. We note that the fitting range (1.57 eV $< \hbar\omega <$ 1.67 eV) determines a carrier temperature close to the room temperature of about (296.7 ± 2.5) K $[(22.5 \pm 2.5)°C]$. We provide an analysis of the fitting sensitivity in Section S4 of the Supporting Information.

Figure 2B displays the back-calculated spectral absorptivity (red line), which exhibits good agreement with the measured spectral absorptivity (black pentagons) in the region unaffected by the edge artefact ($\hbar\omega > 1.57$ eV). This procedure is repeated for each $\phi_{PL}(\hbar\omega)$ curve to determine iV_{OC}.

The $iV_{OC,rad}$ values are determined using Equation (3) together with the determined iV_{OC} and PLQY. Figure 3 illustrates the Suns-PLQY data represented as dark iJ-V curves, where black triangles (circles) represent the dark (radiative) iJ-iV curve. A $\Delta iV_{OC,rad}$ of 30 mV at 1-Sun, caused by NRBR, is indicated by the dashed horizontal line. By fitting the dark radiative iJ-iV curve, we obtain a $J_{0,rad}$ value of (12.2 ± 0.1) yocto-A·cm^{-2} (1 yocto $= 10^{-24}$) using Equation (6). Subsequently, utilising this $J_{0,rad}$ value and Equation (8), we determine a $J_{0,nr}$ value of (36.5 ± 0.5) yocto-A·cm^{-2} from the fit to the dark iJ-iV curve.
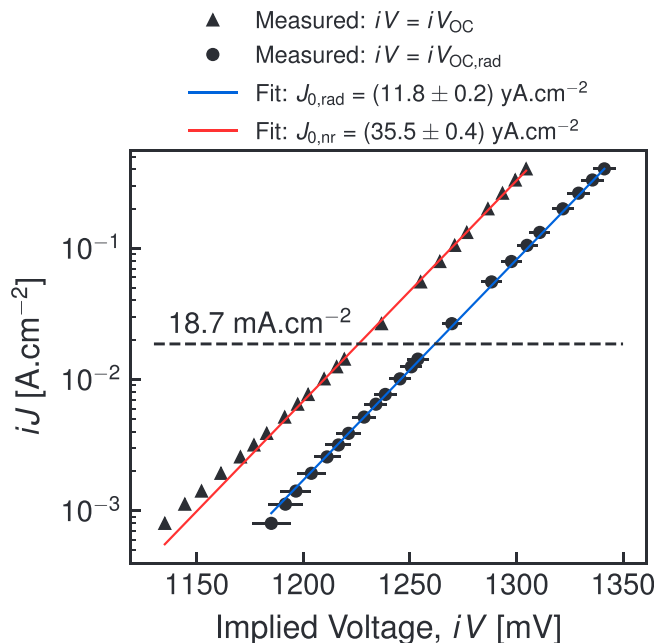
It is important to note that the fitting region for the dark iJ-iV curve is limited to $iV > 1200$ mV. Below this threshold, the curve deviates from Equation (8), likely due to the contribution of other recombination mechanisms such as bulk SRH from mid-gap defects.[31,32] The dark iJ-iV curve fits for the thick and thin PTFs are in Section S5 of the Supporting Information.

Table 2 lists the $J_{0,nr}$ values for PTFs of varying thickness, indicating a slight increase in $J_{0,nr}$ with increasing thickness (less than 33%, see Section S6 of the Supporting Information). If NRBR originates only from the bulk, one would anticipate a nearly tripled $J_{0,nr}$ when transitioning from thin to thick PTFs (469/160 nm $\approx$ 2.93). Conversely, if NRBR arises from the surfaces, $J_{0,nr}$ should be independent of the thickness. The observed modest increase in $J_{0,nr}$ with increasing thickness suggests the presence of a significant surface component combined with a relatively smaller bulk component of $J_{0,nr}$.

FIGURE 2 (A) A linear transform of the 1-Sun $\phi_{PL}(\hbar\omega)$, according to Equation (3) (black triangles) and linear curve fit (solid red line) used to extract iV_{OC} and the temperature. The error bars on the black triangles represent the measurement uncertainty. The shaded red regions represent the effect of the standard errors of iV_{OC} and the temperature on the fit. (B) Reference spectral absorptivity (black pentagons) and back-calculated spectral absorptivity from 1-Sun $\phi_{PL}(\hbar\omega)$ (solid red line). The error bars on the measured spectral absorptivity represent the standard deviation of the absorptivity measured from either side of the PTF/glass stack. The shaded red regions represent the propagated uncertainty in the measured $\phi_{PL}(\hbar\omega)$, and the curve-fitted iV_{OC} and temperature .

FIGURE 3 Dark iJ-iV curves for intermediate PTF. The red (blue) curve is a curve fit to the dark (radiative) iJ-iV curve using Equation (8) (Equation 6). The dashed line represents the 1-Sun J_L, equal to 18.7 mA·cm^{-2}. The horizontal distance between the intersection of the dark iJ-iV curves with this dashed line represents the 1-Sun $\Delta iV_{OC,rad}$.

TABLE 2 $J_{0,nr}$ values obtained from Equations (6) and (8).

Thickness	W (nm)	D_{gb} (nm)	$J_{0,nr}$ (yocto-A·cm^{-2})
Thick	469.3 ± 4.0	203 ± 64	40.6 ± 1.4
Intermediate	262.2 ± 2.0	170 ± 52	36.5 ± 0.5
Intermediate[a]			36.2 ± 0.5
Thin	159.5 ± 5.5	151 ± 55	31.2 ± 0.5
Thin[a]			33.4 ± 0.4
Average	n/A		35.6 ± 10.6

Note: W and D_{gb} values are included for completeness. The average uncertainty is calculated using $\sqrt{\left\langle J_{0,nr}^2 + \triangle J_{0,nr}^2 \right\rangle - \langle J_{0,nr} \rangle^2}$, where $\Delta J_{0,nr}$ is the individual uncertainty of each $J_{0,nr}$ measurement and the brackets indicate the mean value.

[a]Additional measurements on separate locations.

While a bulk $J_{0,nr}$ component could be attributed to SRH recombination[31] from shallow bulk defects,[15] we find that the required N_t is implausibly large (see Section S7 of the Supporting Information). A simpler explanation is relatively minor differences in the SRH recombination parameters[33] among the PTFs of different thicknesses. For instance, a 33% variation in the interface defect density, N_{it}, with the thickness could account for the observed difference. Therefore, the most plausible cause of NRBR are defects at the surfaces, and in this context, the $J_{0,nr}$ parameter is equivalent to $J_{0,s}$ (surface recombination). It should be noted that $J_{0,s}$ represents the cumulative value across both PTF/air and PTF/glass surfaces.

It is important to note that if NRBR originated from the grain boundaries, as has been demonstrated by previous studies linking the grain size with recombination activity,[34] the opposite trend would be expected between $J_{0,nr}$ and the grain boundary diameter, D_{gb} (also listed in Table 2, see Section S6 of the Supporting Information),[35] since the grain boundary area per unit volume of the film is inversely proportional to D_{gb} (see Section S8 of the Supporting Information). Hence, we rule out grain boundaries as the possible spatial origin of $J_{0,nr}$. For a discussion regarding the relevant domain for the grain boundaries (grains versus crystallites), see Section S9 of the Supporting Information.

Typically, surface recombination in PTFs has been specified in terms of the surface recombination velocity, S (cm·s^{-1}).[36,37] Usually, S is specified as injection-independent values, meaning the surface recombination rate is linear with respect to Δn (monomolecular recombination). However, when the surfaces are highly charged, corresponding to strong accumulation or strong inversion, the electron and hole densities at the surfaces are highly asymmetric. This leads to an injection-dependent S more aptly parametrised by the *surface saturation current parameter, $J_{0,s}$*.[33] We note that $J_{0,s}$ is a well-established parameter for crystalline silicon photovoltaics,[38] routinely used to assess the surface passivation quality.[33,39]

Regarding the origin of $J_{0,s}$, we propose two possible mechanisms from the framework of SRH recombination.[31] Both assume a single energy-level surface defect and involve a significant interface band-bending/photovoltage, ψ_s, leading to asymmetric electron and hole densities at the boundary.[33] The first case is near band-edge donor (acceptor) states close to the conduction (valence) band-edge:

$$J_{0,s} = q \cdot c_x \cdot N_{it} \cdot n_i \cdot \exp\left[s\frac{E_t - E_i}{k_B T}\right] \quad (10)$$

where c_x is the capture coefficient with $x = n$ and $s = -1$ ($x = p$ and $s = +1$) for a donor (acceptor), N_{it} is the interface state density (cm^{-2}) and ($E_t - E_i$) is the defect energy level (eV) referenced to the intrinsic energy level. We determine that Equation (10) is a reasonable approximation if the defect energy-level is within 50 meV of the valence (conduction) band-edge, corresponding to excess carrier densities of less than 10^{17} cm^{-3} (see Section S10 for a derivation of Equation 10). This mechanism was previously proposed by Brenes et al.[18] for methylammonium lead triiodide (MAPbI$_3$) and has supporting evidence from Fassl et al. based on analysing the PLQY of different stoichiometries of MAPbI$_3$ under atmospheric light soaking.[40,41] The second case is a mid-gap defect accompanied by a large surface charge, Q_s:[33]

$$J_{0,s} = \frac{q \cdot c_x \cdot N_{it} \cdot 2k_B T \cdot \varepsilon \cdot n_i^2}{Q_s^2} \quad (11)$$

where ε is the permittivity. Q_s could be caused by the accumulation of mobile, charged ions near the surfaces.[42] We performed surface photovoltage mapping on a Br17 sample with in-situ LS, revealing a positive ψ_s of several hundred meV. This indicates the presence of

donor states at the surface, further reinforcing the hypothesis of a significant $J_{0,s}$ (see Section S11 of the Supporting Information). To distinguish which of these two mechanisms is relevant, the temperature-dependence of $J_{0,s}$ can be measured from temperature-dependent Suns-PLQY. Ignoring the temperature dependencies of c_n, Q_s, and ε, which are non-trivial, Equations (10) and (11) have distinct temperature dependencies of $T^{3/2}\cdot\exp(-[E_g(T) + 2\cdot(E_t - E_i)]/2k_BT)$ and $T^4\cdot\exp(-E_g(T)/k_BT)$, respectively, where E_g is the bandgap energy.

Previous studies[35,36] determined an S value by analysing the minority carrier lifetime, τ, under the assumption of a surface recombination rate given by $R_s = S\cdot\Delta n_s$, where R_s denotes the surface recombination rate (cm^{-2}·s^{-1}), and Δn_s represents the excess carrier density near the surface. To verify that the lifetime is predominantly influenced by the surface, several films with varying thicknesses were employed, leading to the following relationship: $\tau = \frac{S}{W} + \frac{1}{\tau_{bulk}}$, where τ_{bulk} represents the bulk lifetime. However, in this current study, $J_{0,s}$ is determined using Suns-PLQY measurements, which assess the energy losses relative to the radiative limit. The $J_{0,s}$ value is predicated on a non-linear surface recombination rate: $R_s = \frac{J_{0,s}}{q}\cdot(n_sp_s - n_i^2)$, where n_s (p_s) denotes the electron (hole) density (cm^{-2}) at the surface. Several films with different thicknesses were investigated to confirm that the recombination predominantly occurs at the surfaces, rather than in the bulk (as represented in Equation 9). It is noteworthy that TR-PL measurements alone cannot be employed to extract $J_{0,s}$ because they solely provide information about the sum of the saturation current densities via the total bimolecular recombination coefficient, B_{tot}: $B_{tot} = \frac{J_{0,s}+J_{0,rad}}{qWn_i^2}$.[15,27] In contrast, the method presented in this study allows for the separation of $J_{0,s}$ and $J_{0,rad}$ without necessitating additional techniques, as expressed in Equations (6) and (8).

5 | CONCLUSIONS

In this study, we have successfully showcased a straightforward and powerful analysis approach utilising Suns-PLQY measurements to quantify non-radiative bimolecular recombination in semiconductor thin films, as well as identify its spatial origin. Notably, we demonstrated that NRBR in the studied PTFs arises from defects located at the surfaces, which can be effectively described by the $J_{0,s}$ parameter. We determined an average $J_{0,s}$ value of (35.6 ± 10.6) yocto-A·cm^{-2} across thicknesses ranging from 160 nm to 470 nm. We propose either band-edge surface defects or mid-gap surface defects coupled with large surface charge as plausible origins of $J_{0,s}$, and suggest using temperature-dependent Suns-PLQY to determine the exact origin of $J_{0,s}$. The application of this simple analysis technique holds potential for the characterisation of $J_{0,s}$ in perovskite compositions and other semiconductor materials.

DATA AVAILABILITY STATEMENT
The data that support the findings of this study are available from the corresponding author upon reasonable request.

ORCID
Robert Lee Chin https://orcid.org/0000-0001-9577-2561
Anita Ho-Baillie https://orcid.org/0000-0001-9849-4755
Thorsten Trupke https://orcid.org/0000-0002-4895-9750
Ziv Hameiri https://orcid.org/0000-0002-2934-4478

REFERENCES
1. Stolterfoht M, Grischek M, Caprioglio P, et al. How to quantify the efficiency potential of neat perovskite films: Perovskite semiconductors with an implied efficiency exceeding 28%. *Adv Mater*. 2020; 32(17):2000080. doi:10.1002/adma.202000080
2. Hages CJ, Redinger A, Levcenko S, et al. Identifying the real minority carrier lifetime in nonideal semiconductors: A case study of kesterite materials. *Adv Energy Mater*. 2017;7(18):1700167. doi:10.1002/aenm.201700167
3. de Mello JC, Wittmann HF, Friend RH. An improved experimental determination of external photoluminescence quantum efficiency. *Adv Mater*. 1997;9(3):230-232. doi:10.1002/adma.19970090308
4. Katahara JK, Hillhouse HW. Quasi-Fermi level splitting and sub-bandgap absorptivity from semiconductor photoluminescence. *J Appl Phys*. 2014;116(17):173504. doi:10.1063/1.4898346
5. Braly IL, deQuilettes DW, Pazos-Outón LM, et al. Hybrid perovskite films approaching the radiative limit with over 90% photoluminescence quantum efficiency. *Nat Photonics*. 2018;12(6):355-361. doi:10.1038/s41566-018-0154-z
6. Frohna K, Anaya M, Macpherson S, et al. Nanoscale chemical heterogeneity dominates the optoelectronic response of alloyed perovskite solar cells. *Nat Nanotechnol*. 2022;17(2):190-196. doi:10.1038/s41565-021-01019-7
7. Wurfel P. The chemical potential of radiation. *J Phys C: Solid State Phys*. 1982;15(18):3967-3985. doi:10.1088/0022-3719/15/18/012
8. Rau U. Reciprocity relation between photovoltaic quantum efficiency and electroluminescent emission of solar cells. *Phys Rev B*. 2007; 76(8):085303. doi:10.1103/PhysRevB.76.085303
9. Caprioglio P, Wolff CM, Sandberg OJ, et al. On the origin of the ideality factor in perovskite solar cells. *Adv Energy Mater*. 2020;10(27): 2000502. doi:10.1002/aenm.202000502
10. Sarritzu V, Sestu N, Marongiu D, et al. Optical determination of Shockley-Read-Hall and interface recombination currents in hybrid perovskites. *Sci Rep*. 2017;7(1):44629. doi:10.1038/srep44629
11. Richter JM, Abdi-Jalebi M, Sadhanala A, et al. Enhancing photoluminescence yields in lead halide perovskites by photon recycling and light out-coupling. *Nat Commun*. 2016;7(1):13941. doi:10.1038/ncomms13941
12. Staub F, Kirchartz T, Bittkau K, Rau U. Manipulating the net radiative recombination rate in lead halide perovskite films by modification of light outcoupling. *J Phys Chem Lett*. 2017;8(20):5084-5090. doi:10.1021/acs.jpclett.7b02224
13. Davies CL, Filip MR, Patel JB, et al. Bimolecular recombination in methylammonium lead triiodide perovskite is an inverse absorption process. *Nat Commun*. 2018;9(1):293. doi:10.1038/s41467-017-02670-2

14. Simbula A, Pau R, Liu F, et al. Direct measurement of radiative decay rates in metal halide perovskites. *Energ Environ Sci*. 2022;15(3):1211-1221. doi:10.1039/D1EE03426J

15. Bowman AR, Macpherson S, Abfalterer A, Frohna K, Nagane S, Stranks SD. Extracting decay-rate ratios from photoluminescence quantum efficiency measurements in optoelectronic semiconductors. *Phys Rev Appl*. 2022;17(4):044026. doi:10.1103/PhysRevApplied.17.044026

16. Staub F, Rau U, Kirchartz T. Statistics of the Auger recombination of electrons and holes via defect levels in the band gap—application to lead-halide perovskites. *ACS Omega*. 2018;3(7):8009-8016. doi:10.1021/acsomega.8b00962

17. Kiligaridis A, Frantsuzov PA, Yangui A, et al. Are Shockley-Read-Hall and ABC models valid for lead halide perovskites? *Nat Commun*. 2021;12(1):3329. doi:10.1038/s41467-021-23275-w

18. Brenes R, Guo D, Osherov A, et al. Metal halide perovskite polycrystalline films exhibiting properties of single crystals. *Joule*. 2017;1(1):155-167. doi:10.1016/j.joule.2017.08.006

19. Hangleiter A. Nonradiative recombination via deep impurity levels in silicon: experiment. *Phys Rev B*. 1987;35(17):9149-9161. doi:10.1103/PhysRevB.35.9149

20. J.A. Woollam Co., Inc. Guide to using WVASE32.

21. Burkhard GF, Hoke ET. Transfer matrix optical modeling. Stanford University, 2011.

22. Fassl P, Lami V, Berger FJ, et al. Revealing the internal luminescence quantum efficiency of perovskite films via accurate quantification of photon recycling. *Matter*. 2021;4(4):1391-1412. doi:10.1016/j.matt.2021.01.019

23. Lasher G, Stern F. Spontaneous and stimulated recombination radiation in semiconductors. *Phys Rev*. 1964;133(2A):A553-A563. doi:10.1103/PhysRev.133.A553

24. Rey G, Spindler C, Babbe F, et al. Absorption coefficient of a semiconductor thin film from photoluminescence. *Phys Rev Appl*. 2018;9(6):064008. doi:10.1103/PhysRevApplied.9.064008

25. el-Hajje G, Momblona C, Gil-Escrig L, et al. Quantification of spatial inhomogeneity in perovskite solar cells by hyperspectral luminescence imaging. *Energ Environ Sci*. 2016;9(7):2286-2294. doi:10.1039/C6EE00462H

26. Tebyetekerwa M, Zhang J, Liang K, et al. Quantifying quasi-Fermi level splitting and mapping its heterogeneity in atomically thin transition metal dichalcogenides. *Adv Mater*. 2019;31(25):1900522. doi:10.1002/adma.201900522

27. Cuevas A. The recombination parameter J_0. *Energy Procedia*. 2014;55:53-62. doi:10.1016/j.egypro.2014.08.073

28. Altermatt PP, Schenk A, Geelhaar F, Heiser G. Reassessment of the intrinsic carrier density in crystalline silicon in view of band-gap narrowing. *J Appl Phys*. 2003;93(3):1598-1604. doi:10.1063/1.1529297

29. Slotcavage DJ, Karunadasa HI, McGehee MD. Light-induced phase segregation in halide-perovskite absorbers. *ACS Energy Lett*. 2016;1(6):1199-1205. doi:10.1021/acsenergylett.6b00495

30. Kirchartz T, Márquez JA, Stolterfoht M, Unold T. Photoluminescence-based characterization of halide perovskites for photovoltaics. *Adv Energy Mater*. 2020;10(26):1904134. doi:10.1002/aenm.201904134

31. Shockley W, Read WT. Statistics of the recombinations of holes and electrons. *Phys Rev*. 1952;87(5):835-842. doi:10.1103/PhysRev.87.835

32. Hall RN. Electron-hole recombination in germanium. *Phys Rev*. 1952;87(2):387. doi:10.1103/PhysRev.87.387

33. McIntosh KR, Black LE. On effective surface recombination parameters. *J Appl Phys*. 2014;116(1):014503. doi:10.1063/1.4886595

34. Listorti A, Juarez-Perez EJ, Frontera C, et al. Effect of mesostructured layer upon crystalline properties and device performance on perovskite solar cells. *J Phys Chem Lett*. 2015;6(9):1628-1637. doi:10.1021/acs.jpclett.5b00483

35. Yang M, Zeng Y, Li Z, et al. Do grain boundaries dominate non-radiative recombination in $CH_3NH_3PbI_3$ perovskite thin films? *Phys Chem Chem Phys*. 2017;19(7):5043-5050. doi:10.1039/C6CP08770A

36. Wang J, Fu W, Jariwala S, Sinha I, Jen AK-Y, Ginger DS. Reducing surface recombination velocities at the electrical contacts will improve perovskite photovoltaics. *ACS Energy Lett*. 2019;4(1):222-227. doi:10.1021/acsenergylett.8b02058

37. Yang Y, Yang M, Moore DT, et al. Top and bottom surfaces limit carrier lifetime in lead iodide perovskite films. *Nat Energy*. 2017;2(2):16207. doi:10.1038/nenergy.2016.207

38. Kane DE, Swanson RM. Measurement of the emitter saturation current by a contactless photoconductivity decay method. In *18th IEEE Photovoltaic Specialist Conference*. 1985:578–583.

39. Niewelt T, Steinhauser B, Richter A, et al. Reassessment of the intrinsic bulk recombination in crystalline silicon. *Sol Energy Mater Sol Cells*. 2022;235:111467. doi:10.1016/j.solmat.2021.111467

40. Fassl P, Zakharko Y, Falk LM, et al. Effect of density of surface defects on photoluminescence properties in $MAPbI_3$ perovskite films. *J Mater Chem C*. 2019;7(18):5285-5292. doi:10.1039/C8TC05998E

41. Fassl P, Lami V, Bausch A, et al. Fractional deviations in precursor stoichiometry dictate the properties, performance and stability of perovskite photovoltaic devices. *Energ Environ Sci*. 2018;11(12):3380-3391. doi:10.1039/C8EE01136B

42. Gets DS, Verkhogliadov GA, Danilovskiy EY, Baranov AI, Makarov SV, Zakhidov AA. Dipolar cation accumulation at the interfaces of perovskite light-emitting solar cells. *J Mater Chem C*. 2020;8(47):16992-16999. doi:10.1039/D0TC02654A

SUPPORTING INFORMATION

Additional supporting information can be found online in the Supporting Information section at the end of this article.